This article has dealt solely with the application of natural-neighbour theory to the weighted residual method for solving PDEs. We expect that many other applications of natural neighbours will appear in the future. For example, it may well be possible to generalize classical finite-difference methods (which rely on estimating derivatives at nodes of a regular grid[1]) to irregular meshes. Although the natural-neighbour coordinates themselves cannot be used to estimate derivatives at nodes, an extension described by Sibson[12] does give first-order derivatives at the nodes. Because most numerical methods are based on the discretization of a field onto a mesh, the theory of natural neighbours raises the exciting possibility of generalizing methods commonly restricted to regular grids to a Delaunay mesh based on any irregular distribution of nodes. □

Received 27 February; accepted 27 July 1995.

1. Roache, P. J. *Computational Fluid Dynamics* (Hermosa, Albuquerque, NM, 1982).
2. Zienkiewicz, O. C. *The Finite Element Method* 3rd edn (McGraw-Hill, Maidenhead, 1977).
3. Zienkiewicz, O. C. & Phillips, D. V. *Int. J. num. Meth. Engng* **8,** 519–528 (1971).
4. Bathe, K.-J., Ramm, E. & Wilson, E. L. *Int. J. num. Meth. Engng* **9,** 353–386 (1975).
5. Sibson, R. *Math. Proc. Camb. phil. Soc.* **87,** 151–155 (1980).
6. Voronoi, M. G. *J. reine angew. Math.* **134**, 198–287 (1908).
7. Delaunay, B. N. *Bull. Acad. Sci. USSR: Class. Sci. Math.* **7,** 793–800 (1934).
8. Fortune, S. in *Computing in Euclidean Geometry* (eds Du, D. Z. & Hwang, F.) (World Scientific, Singapore, 1992).
9. Barber, B., Dobkin, D. P. & Huhdanpaa, H. *Technical Rep. GCG53* (The Geometry Centre, Univ. Minesota, Minneapolis, 1993).
10. Fortune, S. *Algorithmica* **2,** 153–174 (1987).
11. Braun, J. & Sambridge, M. *Earth planet Sci. Lett.* **124,** 211–220 (1994).
12. Sibson, R. in *Interpreting Multivariate Data* (ed. Barnet, V.) 21–36 (Wiley, Chichester, 1981).
13. Watson, D. F. *Contouring: a Guide to the Analysis and Display of Spatial Data* (Pergamon, Oxford, 1992).
14. Finlayson, B. A. *The Method of Weighted Residuals and Variational Principles* (Academic, New York, 1972).
15. Sambridge, M., Braun, J. & McQueen, H. *Geophys. J. int.* (in the press).
16. Lasserre, J. B. *J. Opt. Theory Applic.* **39,** 363–377 (1983).
17. Bathe, K.-J. *Finite Element Procedures in Engineering Analysis* (Prentice-Hall, Englewood Cliffs, NJ, 1982).
18. Van Norton, R. in *Mathematical Methods for Digital Computers* Vol. 1 (eds Ralston, A. & Wilf, H. S.) (Wiley, New York, 1960).
19. Hughes, T. J. R., Winget, J., Levit, T. & Tedzuyar, T. E. in *Computer Methods for Non-linear Solids and Structure* (eds Atluri, S. N. & Perrone, N.) 75–109 (Am. Soc. Mech. Eng., New York, 1983).
20. Batchelor, G. K. *An Introduction to Fluid Dynamics* (Cambridge Univ. Press, 1967).
21. Fung, Y. C. *Foundations of Solid Mechanics* (Prentice-Hall, Englewood Cliffs, NJ, 1965).

SUPPLEMENTARY INFORMATION. Requests should be addressed to Mary Sheehan at the London editorial office of *Nature*.

ACKNOWLEDGEMENTS. We thank H. McQueen, K. Lambeck and D. Watson for stimulating discussions, U. Christensen for his review and D. Whitehouse for producing the 3D ray-traced pictures.

# Structure at 2.8 Å resolution of cytochrome *c* oxidase from *Paracoccus denitrificans*

**So Iwata, Christian Ostermeier, Bernd Ludwig* & Hartmut Michel†**

Max-Planck-Institut für Biophysik, Heinrich-Hoffmann-Strasse 7, D-60528 Frankfurt/M., Germany * Johann-Wolfgang-Goethe Universität, Biozentrum, Institut für Biochemie, Molekulare Genetik, Marie-Curie-Strasse 9, D-60439 Frankfurt/M., Germany

**The crystal structure at 2.8 Å resolution of the four protein subunits containing cytochrome *c* oxidase from the soil bacterium *Paracoccus denitrificans*, complexed with an antibody $F_v$ fragment, is described. Subunit I contains 12 membrane-spanning, primarily helical segments and binds haem *a* and the haem $a_3$–copper B binuclear centre where molecular oxygen is reduced to water. Two proton transfer pathways, one for protons consumed in water formation and one for 'proton pumping', could be identified. Mechanisms for proton pumping are discussed.**

Cytochrome *c* oxidase, a protein complex located in the inner membrane of mitochondria and many bacteria, is the terminal enzyme of most respiratory chains. It catalyses the final electron transfer steps from cytochrome *c* to molecular oxygen, and is a member of the superfamily of haem–copper containing terminal oxidases (see refs 1–3 for review). In addition to the four protons consumed in water formation per oxygen molecule, up to four protons are electrogenically translocated ('pumped') across the membrane leading to a difference between the two sides of the membrane of the electrochemical potential of protons. This difference can be used to drive the synthesis of adenosine 5′-triphosphate from adenosine 5′-diphosphate and inorganic phosphate.

Protein subunit (SU) I of most cytochrome *c* oxidases contains two haem A molecules, called haem *a* and haem $a_3$, and copper B ($Cu_B$). Haem $a_3$ and $Cu_B$ form a binuclear centre where molecular oxygen is reduced to water. Electrons from cytochrome *c* are first transferred to the copper A centre ($Cu_A$), which is located in protein SU II, and from there to haem *a* and the binuclear centre. The function of SU III, which is present in all mitochondrial and most bacterial terminal oxidases, is unknown. Up to ten small additional subunits are present in mitochondrial cytochrome *c* oxidases[4].

† To whom correspondence should be addressed.

As a prerequisite for understanding the molecular mechanism of oxygen reduction and its coupling to proton pumping, we have determined at 2.8 Å resolution the structure of the four protein subunits containing cytochrome *c* oxidase[5] from the soil bacterium *Paracoccus denitrificans* by X-ray crystallography. This became possible by cocrystallizing this membrane protein complex with an $F_v$ fragment of a monoclonal antibody. Here we describe the structure of this cytochrome *c* oxidase, its protein subunits, the arrangement and mode of binding of the prosthetic groups, and two possible pathways for protons, one for pumped protons and one for protons consumed in water formation. Finally, we discuss mechanisms of proton pumping.

## Structure determination

The fully oxidized cytochrome *c* oxidase from *Paracoccus denitrificans*, complexed with the antibody $F_v$ fragment 7E2, has been crystallized in the presence of 0.1% sodium azide; azide inhibits the enzyme by binding to $Cu_B$ (ref. 6). Data collection, the quality of data and initial phases determined by multiple isomorphous replacement and anomalous scattering are summarized in Table 1. The phases were improved using a series of density modification methods. The refined structural model contains the following 1,329 residues: SU I, 17–554; SU II, 1–252; SU III, 1–273; SU IV, 10–56; $V_L$ chain of the $F_v$ frag-

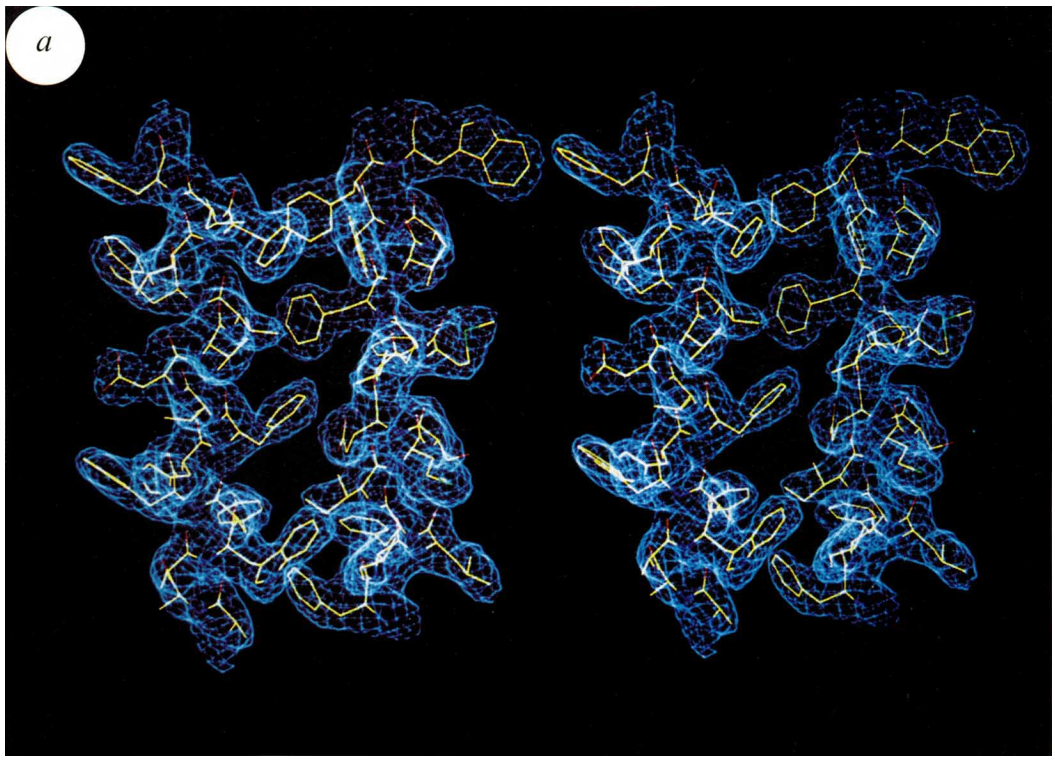


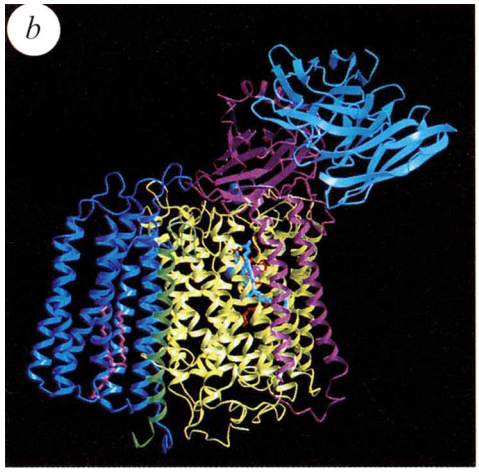


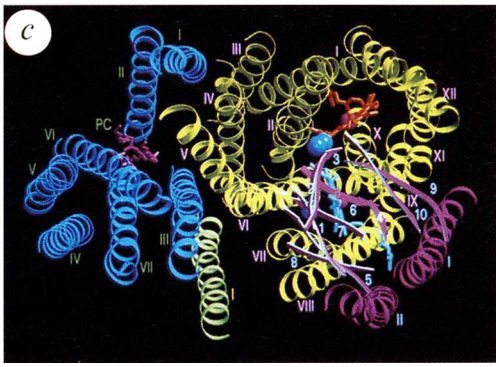


FIG. 1 The three-dimensional structure of cytochrome *c* oxidase. *a*, Representative part of the electron density map corresponding to parts of two transmembrane helices of subunit III. The $2|F_o| - |F_c|$ map was calculated at 2.8 Å resolution and contoured at $1.5\sigma$ (standard deviations above the mean density of the map). *b*, The entire cytochrome *c* oxidase from *Paracoccus denitrificans* complexed with an antibody $F_v$ fragment viewed parallel to the membrane. The polypeptide backbones of subunits I, II, III and IV and the $F_v$ fragment are shown in yellow, magenta, blue, green and cyan, respectively. Subunit I contains two haem A molecules, called haem *a* (red) and haem $a_3$ (cyan), and copper B ($Cu_B$, blue). Subunit II contains the copper A centre ($Cu_A$) consisting of two copper atoms (blue). In subunit III, a firmly bound phospholipid molecule (magenta) is observed. It was modelled as dilauroyl-phosphatidyl choline (PC). *c*, View of the transmembrane helices (with Roman numbers) and the β-strands (with Arabic numbers) of cytochrome *c* oxidase along the membrane normal from the periplasmic side. The colouring is as above. Only subunit II contains extended β-strands. The icon shows the arrangement of the subunits in a more schematic manner for clarity. The sequence numbers of the secondary structure elements are given in the legends of the figures showing the individual subunits. Secondary structures were assigned using the program DSSP[43]; *a* was prepared with the program O[39]; the other figures were produced using the programs MOLSCRIPT[44] and RASTER3D[45,46].

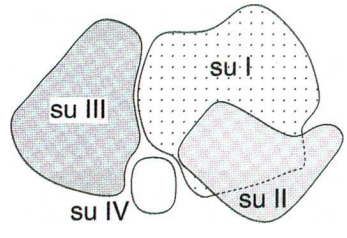


ment, 1–108; and VH chain, 1–120. Three copper atoms, two haem A, and one phosphatidyl choline molecule are included in the current model. A representative part of the electron density map for the refined structure at 2.8 Å resolution is shown in Fig. 1*a*.

## Architecture of cytochrome *c* oxidase

A general view of the *Paracoccus denitrificans* cytochrome *c* oxidase parallel to the membrane is shown in Fig. 1*b*. In projection the part integrated into the membrane has a trapezoidal appearance. The width at the bottom which corresponds to the cyto-

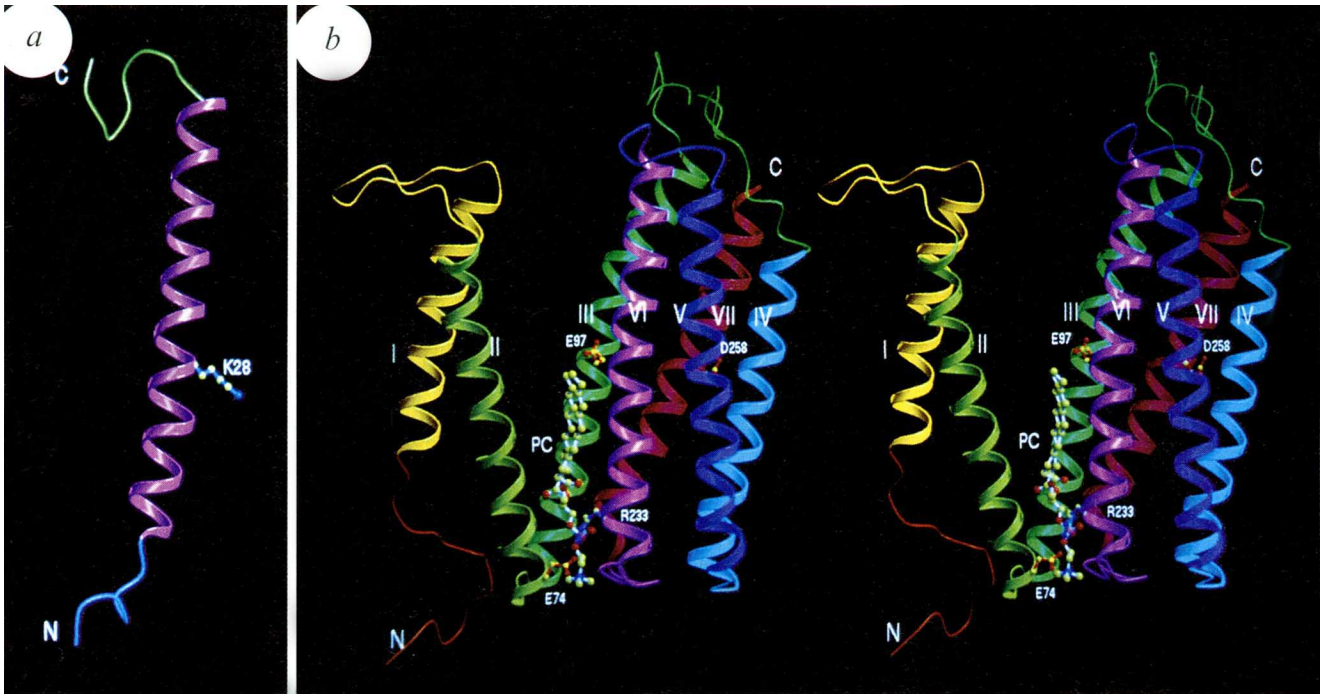


FIG. 2 Structures of subunits III and IV. *a*, View of subunit IV parallel to the membrane. One basic residue, SU IV–Lys 28, is found within the transmembrane helix (SU IV–TM I, residues 16–47). *b*, Stereo view of subunit III as seen parallel to the membrane. The subunit contains 7 transmembrane helices (SU III–TM I, 15–35; II, 48–76; III, 79–114; IV, 139–165; V, 168–196; VI, 203–236 and VII, 244–273). The firmly bound putative phosphatidyl choline molecule is indicated by PC. The alkyl chains of the lipid are visible up to a length of 12 carbon atoms only. The conserved amino acid residues SU III–Arg 233 and SU III–Glu 74, which form ion pairs with the phosphate and the quaternary ammonium groups of the lipid head group, respectively, and two acidic residues in the transmembrane helices (SU III–Glu 97 and SU III–Asp 258) are also shown.

plasmic surface, is ~90 Å; at the top, which represents the periplasmic surface, it is ~75 Å. The height of the trapezoid is 55 Å. It comprises 22 membrane-spanning, primarily helical segments and their connections. The globular domain of SU II (see below) is attached to the trapezoid from the top, resulting in a maximum height of 95 Å. The central part of the complex is made up by SU I which binds both haems and $Cu_B$. Subunit I is associated with SU II at one side and SU III at the other. The amino and carboxy termini of subunit II protrude into the periplasmic space and form a globular domain which contains $Cu_A$. The antibody fragment, which is also shown in Fig. 1*b*, binds to this globular domain. SU IV consists mainly of one transmembrane helix, but it is nevertheless in contact with the other three subunits (see below). When viewed along the membrane normal, cytochrome *c* oxidase has an oval shape with largest dimensions of 90 and 60 Å (Fig. 1*c*).

## Protein subunits and prosthetic groups

**Subunit IV.** The function of this small subunit is unknown. Its discovery in *Paracoccus* cytochrome *c* oxidase is comparatively recent, and only the sequence of the N-terminal 31 residues has been published[5]. Residues 10–56 are visible in our electron density map. The subunit consists mainly of one transmembrane helix (residues 16–47) with the N terminus on the cytoplasmic side (Fig. 2*a*). As an unexpected feature, one lysine residue is found in the transmembrane helix at position 28. Subunit IV is in contact with all other subunits. The nine C-terminal residues touch residues of three transmembrane (TM) helices (SU III–TM III, SU I–TM VII, SU I–TM VIII). The residue SU II–Arg 198 forms a salt bridge with the C-terminal carboxy group of SU IV. The upper part of the transmembrane helix has indirect contacts with SU III mediated by a presumed phospholipid which is only partially visible in the electron density map and is not included in the model. Recently, the gene coding for SU IV has been cloned (H. Witt and B.L., unpublished). The available sequences indicate that SU IV is the N-terminal part of a larger (pro) protein of unknown function. However, SU IV is not a typical leader peptide; it may stabilize the *Paracoccus* cytochrome *c* oxidase.

**Subunit III.** The function of this subunit is also unknown. It does not contribute to the binding of the redox-active prosthetic groups. nor is it involved in proton pumping, as a two-subunit cytochrome *c* oxidase consisting of SU I and II can be isolated[7], and is active in proton pumping[8]. SU III may be involved in the assembly of the cytochrome *c* oxidase[9]. It possesses seven transmembrane helices that are arranged in an irregular manner. When viewed from the periplasmic space and counted clockwise, the order is I, III, VII, IV, V, VI and II (see Fig. 1*c*). The seven transmembrane helices are divided into two bundles, one formed by the first two helices, and the other by the transmembrane helices III to VII. The two bundles are separated by a large V-shaped cleft (Fig. 2*b*), at the bottom of which one lipid molecule is firmly bound. The electron density is compatible with phosphatidyl choline in a syn-clinal/β/anti-periplanar conformation (see ref. 10 for definition). The conserved amino acid residues SU III–Arg 233 and SU III–Asp 74 form ion pairs with the phosphate and the quaternary ammonium of the lipid head group, respectively. The alkyl chains of the lipid, which are not visible in full lengths, are lined up in the cleft along helices III and VI. The well-conserved dicyclohexyl carbodiimide binding residue SU III–Glu 97 (ref. 11) is located in the centre of the third transmembrane helix near the cleft. It is therefore probably protonated and forms a hydrogen bond with the conserved SU III–His 219. Its role may be structural.

The cleft of SU III may be a docking site for other membrane proteins. The membrane-anchored cytochrome $c_{552}$ seems to be a physiological electron donor to $Cu_A$ of the *Paracoccus* cytochrome *c* oxidase[12]. Its membrane anchor would fit into the cleft,

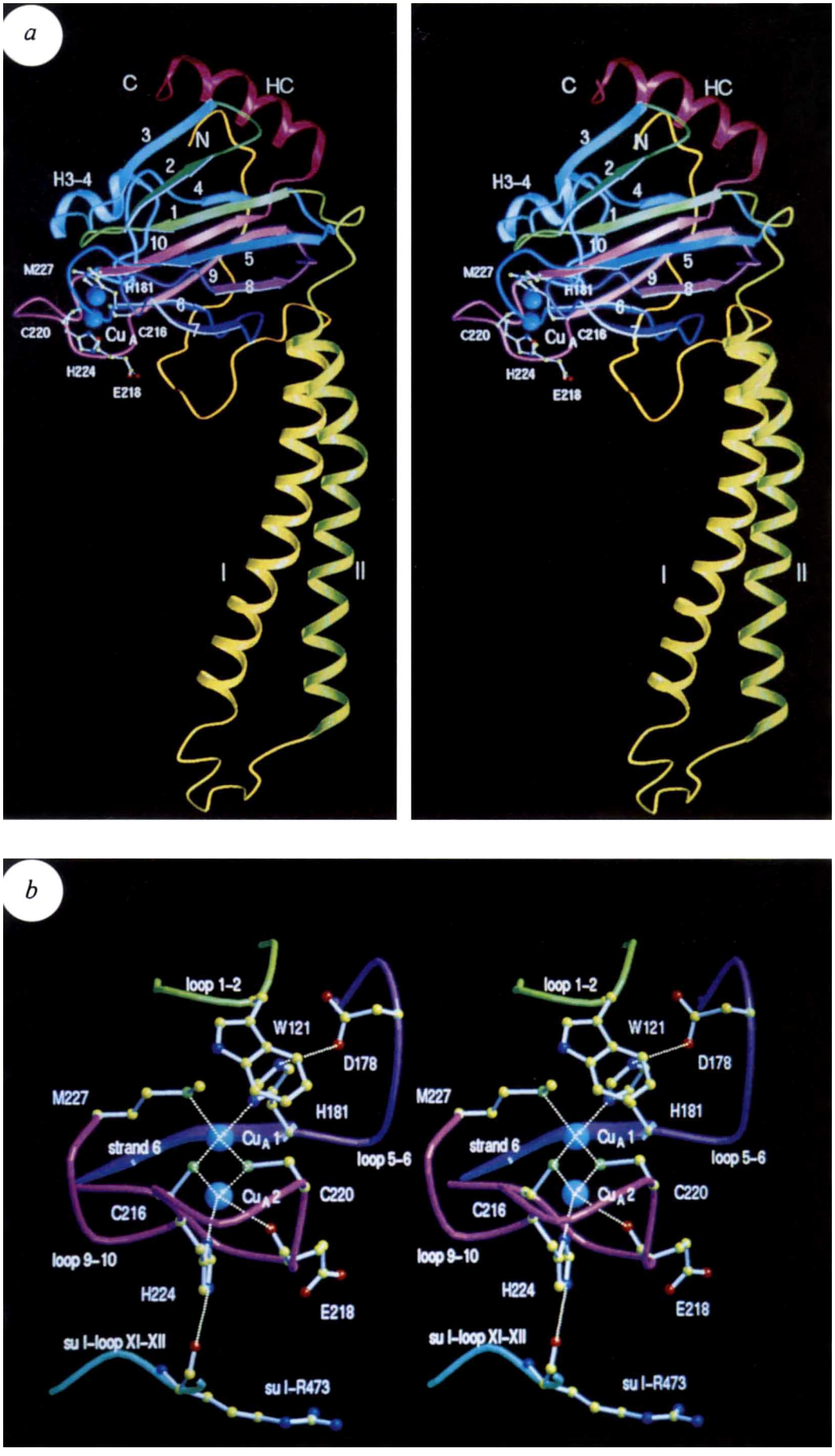


FIG. 3 Structure of subunit II. *a*, Stereo view of subunit II approximately parallel to the membrane. The N-terminal loop (residues 1–26), two transmembrane helices (SU II–TM I, residues 27–59; and II, residues 74–105), including their connection (residues 60–73) and a C-terminal globular domain (residues 106–252) which contains the $Cu_A$ centre are shown. The C-terminal globular domain contains a 10-stranded β-barrel (strand 1, residues 114–119; 2, 123–127; 3, 132–136; 4, 162–164; 5, 169–175; 6, 181–185; 7, 190–194; 8, 200–204; 9, 209–216 and 10, 227–234), and two helices, helix 3–4 (H3–4, residues 140–147) and a C-terminal helix (HC, residues 235–249). The two copper atoms (blue) of the $Cu_A$ centre and their ligands are shown. *b*, Stereo view of the $Cu_A$ centre. The loops providing ligands to the copper atoms are shown and named according to the β-strands which they connect.

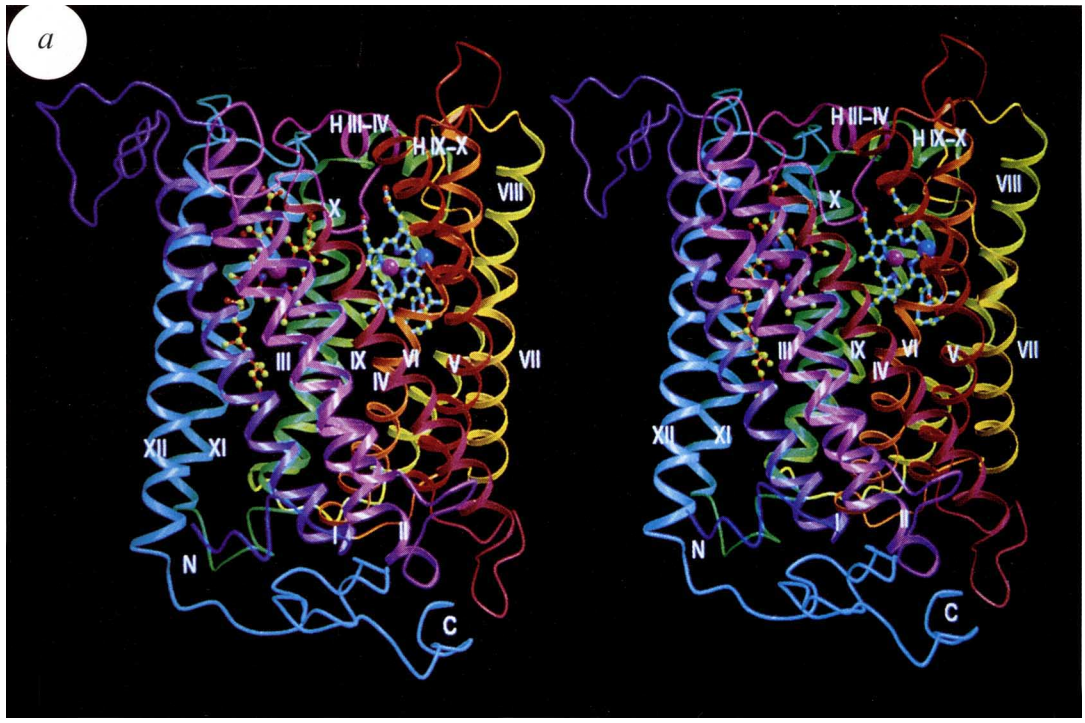


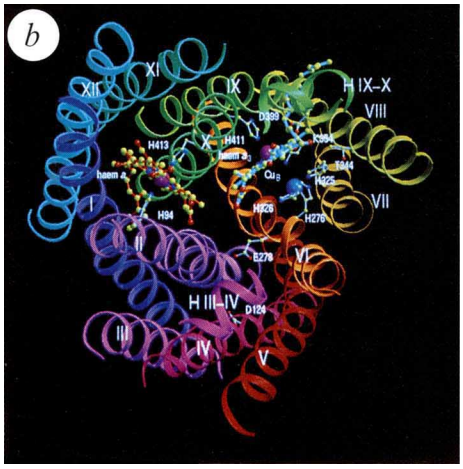


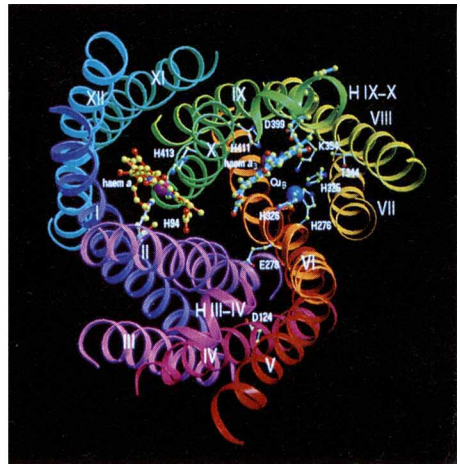


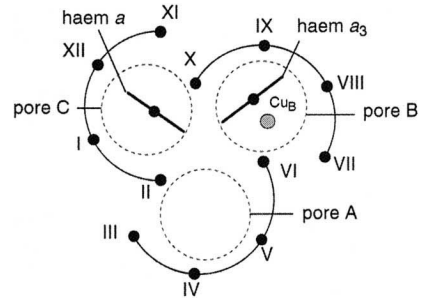


and its globular domain might be in an appropriate position to transfer electrons to $Cu_A$.

**Subunit II.** Subunit II comprises three segments: an N-terminal loop (residues 1–26), two transmembrane helices, including their connection (SU II–TM I and SU II–TM II, residues 27–105), and a C-terminal globular domain (residues 106–252) which contains $Cu_A$ (Fig. 3*a*). The N-terminal loop and C-terminal domain interact tightly on the periplasmic side. Both are located above pore B of SU I (see below). The transmembrane helices SU II–TM I and SU II–TM II are in extensive contact with two transmembrane helices of SU I (SU I–TM IX and SU I–TM VIII, respectively; Fig. 1*c*).

The folding of the C-terminal globular domain containing a ten-stranded β-barrel is similar to that of class I copper proteins such as plastocyanin and azurin, as expected from sequence comparisons[2,13,14]. The α-carbon atoms of the core region superimpose on plastocyanin[15] with a root mean square difference of 2.2 Å for 74 of the 99 plastocyanin residues. The major difference is the insertion of strands 3 and 4 and the loop between these strands in SU II.

As an important difference to the type I copper proteins, $Cu_A$ has been suggested to be a mixed-valence [Cu(1.5)–Cu(1.5)] complex[16–20], which agrees with the crystal structure (Fig. 3*b*). The binding site for the two copper atoms ($Cu_A1$ and $Cu_A2$) is formed by residues from strand 6 and the loop connecting strands 9 and 10 (Fig. 3*b*). The ligands of $Cu_A1$ are the residues SU II–Cys 216, SU II–Cys 220, SU II–His 181 and SU II–Met 227; those of $Cu_A2$ are SU II–Cys 216, SU II–Cys 220, Su II–His 224 and the carbonyl oxygen of SU II–Glu 218 (Fig. 3*c*). The ligands for each Cu atom form a distorted tetrahedron. The two copper atoms are bridged by two cystein thiolates. In our model the Cu–Cu distance is 2.6 Å. The copper and the sulphur atoms lie in one plane. The Cu–$S_\gamma$ (Cys), Cu–$S_\delta$ (Met), Cu–$N_{\delta1}$ (His) and Cu–O (Glu) distances are 2.3, 2.7, 2.1–2.2 and 3.0 Å, respectively. The Cu–$S_\gamma$ (Cys) distances are difficult to determine because overlap of the electron densities of the copper and sulphur atoms makes it difficult to locate the sulphur atoms precisely. The bond lengths for Cu–$S_\delta$ and Cu–O are similar to those observed in type I copper proteins[13].

The residue SU II–Trp 121, which is within 3.2 Å of SU II–Met 227, might be involved in electron transfer from cytochrome *c* to $Cu_A$. SU II–Trp 121 and SU II–Asp 178, which can form a hydrogen bond to the Cu-ligand SU II–His 181, shield the $Cu_A$ centre from the solvent. Very close to this site, is the most likely cytochrome *c* binding site, the corner formed by the globular domain of SU II and the flat periplasmic surface of SU I (Fig.

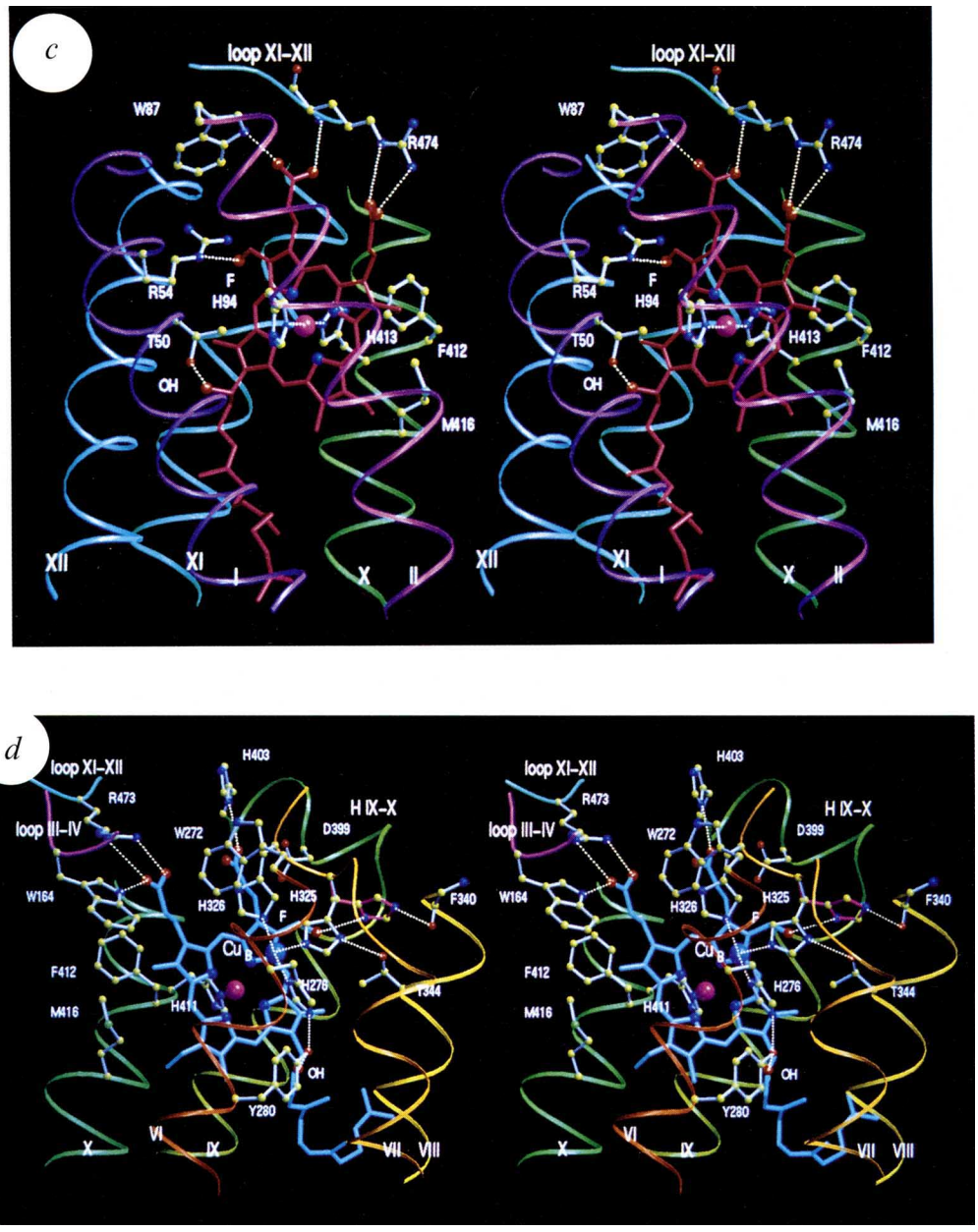


FIG. 4 Structure of subunit I. *a*, Stereo view of subunit I parallel to the membrane. The subunit contains 12 partly interrupted transmembrane helices (SU I–TM I, residues 27–59; II, 84–121; III, 130–151; IV, 178–206; V, 218–251; VI, 263–298; VII, 304–322; VIII, 334–362; IX, 370–395; X, 404–430; XI, 441–468 and XII, 483–513) and two helices parallel to the membrane (helix III–IV, residues 167–174, and helix IX–X, 396–403). Haem *a* (red), haem $a_3$ (cyan) and $Cu_B$ (blue sphere) are also shown. *b*, Stereo view of subunit I along the membrane normal from the periplasmic side. Only the helices are shown together with some important residues. The icon shows schematically the arcs of helices and pores A, B and C formed by them. *c*, Stereo view of haem *a* and surrounding amino acid residues. The symbols OH and F indicate hydroxyl and formyl groups of haem A, respectively. *d*, Stereo view of the binuclear centre of haem $a_3$ and $Cu_B$. The side chain of SU I–His 325 may possess two alternative conformations: in one (white) the side chain forms a bond to $Cu_B$ and a hydrogen bond to Su I–Thr 344, and in the other (red) it forms hydrogen bonds to the formyl group of haem $a_3$ and the carbonyl oxygen of SU I–Phe 340.

1*b*). A part of the loop connecting transmembrane helices III–IV of SU III might also be involved in docking cytochrome *c*. This area contains 10 acidic residues which could interact with lysine residues on the surface of cytochrome *c* (ref. 21).

SU II–His 224 might be involved in electron transfer to haem *a*. The $N_{\varepsilon 2}$ atom of this histidine could donate a hydrogen to the carbonyl oxygen of SU I–Arg 473 in loop XI–XII of SU I. Several residues of this loop are in contact with the propionate groups of haem *a*. The distance from the conjugated π-electron system of SU II–His 224 to that of haem *a* is 11.9 Å, whereas it is 15.4 Å to that of haem $a_3$. The distances from the lower $Cu_A$-atom to the haem *a* Fe is 19.5, to the haem $a_3$ Fe is 22.1 Å. The shorter distances to haem *a* are in agreement with the observed direct electron transfer from $Cu_A$ to haem *a*.

**Subunit I.** SU I contains 12 membrane spanning segments, SU I–TM I to SU I–TM XII, with preferentially helical secondary structure (Fig. 4*a*). It shows an unexpected approximate threefold rotational symmetry. When viewed from the periplasmic side, the 12 segments appear to form three symmetry related semicircular arcs with segments II, VI and X being closest to the rotation axis, and segments XI, III and VII most distant (Fig. 4*b*). The order of the helices is sequential in an anticlockwise manner. Segments XI, XII, I and II form the first semicircle II–VI the second, and VII–X the third. The semicircles together with the last segment of the previous semicircle have a pore-like appearance. In such a description, 'pores' A, B and C are formed by transmembrane segments II–VI; VI–X; and X–XII, I and II, respectively. Segments II, VI and X are part of the walls of two pores each. The 'pores' are blocked, pore A by mostly conserved aromatic residues, pore B by haem $a_3$ and $Cu_B$, and pore C by haem *a* and its hydroxyethylfarnesyl side chain (see also Fig. 4*c*). The membrane-spanning segments are connected by 11 loops referred to as SU I–loop I–II to SU I–loop XI–XII. In general, the loops on the periplasmic side are longer (8–26 residues) than those on the cytoplasmic side (5–10 residues). Long periplasmic loops fold back into the subunit so that a flat surface is generated. Only SU I–loops III–IV and IX–X contain short helices which are parallel to the membrane plane. Loop I–II contains a non-conserved disulphide bridge formed by SU I–Cys 66 and SU I–Cys 80. The N and C termini are on the cytoplasmic side. The N-terminal 16 residues are disordered and not visible in the electron density map; the C-terminal 41 residues are of

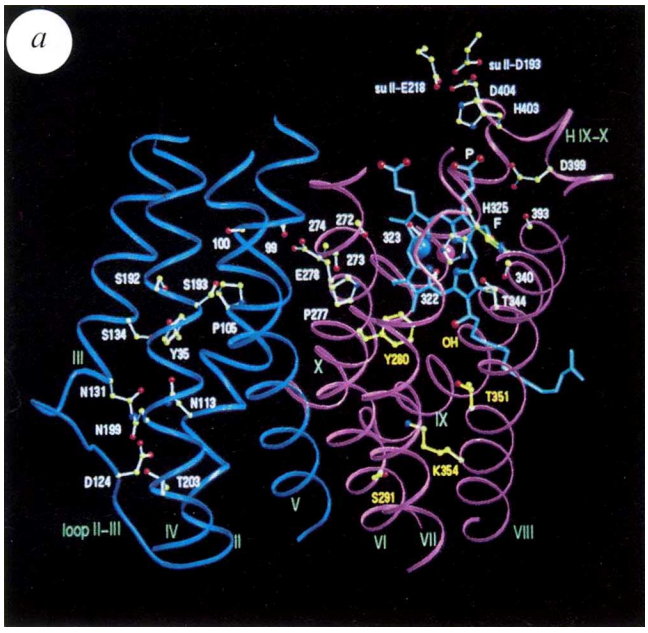


FIG. 5 Proton pathways and possible mechanism of proton pumping. *a*, The proton pathways in subunit I. Residues in the pathway for pumped protons and protons consumed in water formation are labelled in white and yellow, respectively. Two alternative conformations of SU I–His 325 are shown in white and green, respectively. Residues in the negative charge cluster, which is a possible Mn/Mg binding site, are labelled in blue. Important backbone carbonyl groups are labelled with the sequence number only. The symbols OH, F and P indicate hydroxyl, formyl and propionate groups, respectively, of haem $a_3$. The segments forming pore A are shown in blue, except for segment SU I–TM VI, those forming pore B in purple. *b*, Schematic representation of the proton pathways and the histidine shuttle. The thick broken lines represent possible proton pathways. *c*, Histidine cycle/shuttle mechanism for coupling of proton pumping to oxygen reduction to water (short version). The numbers above the boxes describe the states referred to in the text. The symbols are as follows: O, fully oxidized; A, the compound A; P, the peroxy; and F, the oxoferryl (F) states[1,30]. Protons to be pumped enter the boxes at the bottom right and leave at the top along the broken arrows. They are indicated in bold. Protons to be consumed enter from the lower left. Movements of the SU I–His 325 side chain ('Im') are indicated by the short white arrows in the boxes.

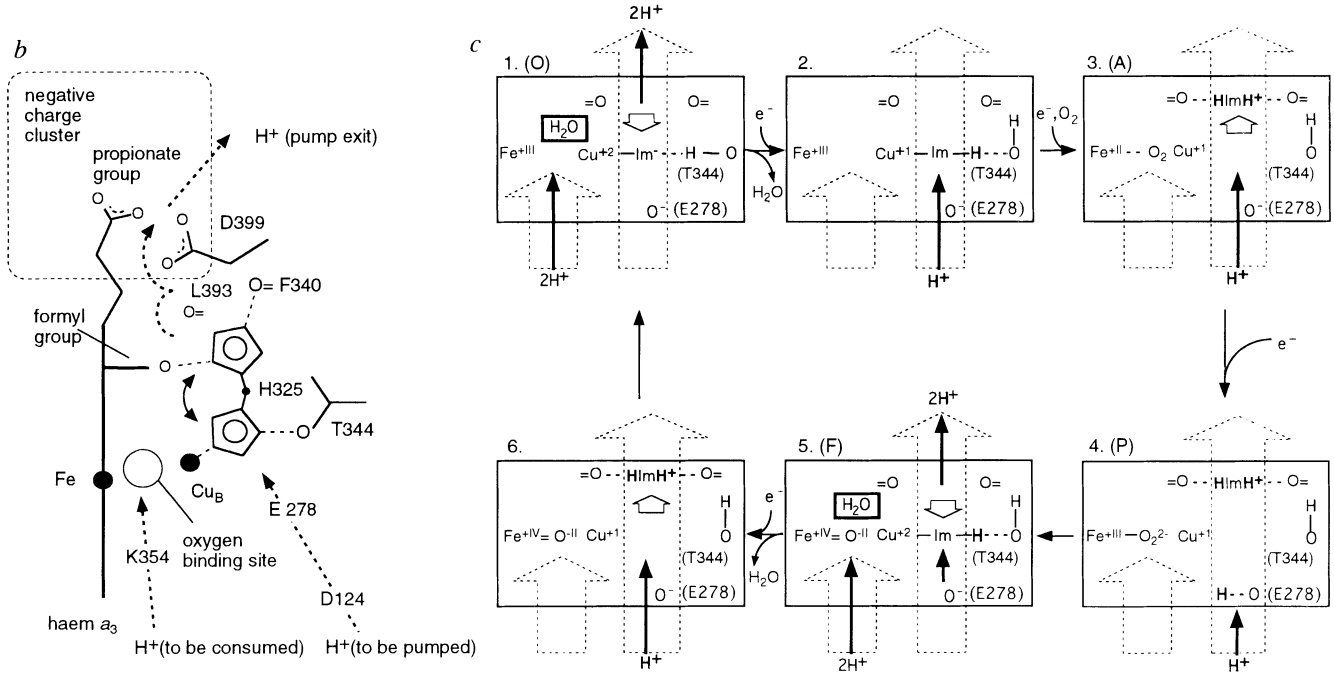


extended secondary structure with turns and form the bottom of SU I.

**Haem *a*.** Haem *a* is a low-spin haem with two histidine residues as axial Fe-ligands. It transfers electrons from $Cu_A$ to the binuclear centre. The haems are characterized by non-covalent binding to the protein and the presence of a formyl group at C8 and a hydrophobic hydroxyethylfarnesyl group at C2 (Fig. 4*c*). The axial Fe-ligands of this haem are His 94 from SU I–TM II and His 413 from SU I–TM X as predicted[22]. The haem *a* formyl group accepts a hydrogen bond from the side chain of SU I–Arg 54. The propionate groups of haem *a* are connected with the $Cu_A$ centre by SU I–loop XI–XII. The side chain of SU I–Arg 474 apparently forms a hydrogen bond/ion pair with one of the two propionates, the other propionate is hydrogen bonded to the peptide carbonyl oxygen of SU I–Arg 474 and the side chain of SU I–Trp 87. In contrast to haem $a_3$, the hydroxyethylfarnesyl group of haem *a* remains in pore C. It is tightly surrounded by hydrophobic residues, so access to haem *a* from the cytoplasmic side is completely blocked.

**Haem $a_3$ and $Cu_B$.** The binuclear centre formed by haem $a_3$ and $Cu_B$ is the catalytic centre for $O_2$ reduction. it is located in pore B, but residues of loops III–IV, XI–XII and the horizontal helix in loop IX–X also contribute. The haem $a_3$ Fe appears to be fivefold coordinated with SU I–His 411 from SU I–TM X as an axial protein ligand. The Fe is ~0.7 Å out of the haem plane towards the histidine. All the polar groups of the haem seem to form hydrogen bonds or salt bridges (see Fig. 4*d* for details). The hydroxyethylfarnesyl group leaves pore B and penetrates into the lipid bilayer to allow access of protons from the cytoplasmic space (see below). The $Cu_B$ ion is 5.2 Å away from the haem $a_3$ iron. Molecular oxygen is supposed to bind between the haem $a_3$ Fe and $Cu_B$. The electron density map indicates the presence of a solvent (or azide) molecule there. SU I–His 276 ($N_{\delta 1}$) and SU I–His 326 ($N_{\varepsilon 2}$) are $Cu_B$-ligands. The residue

TABLE 1 Statistics for X-ray data collection and phase determination

(*a*) Diffraction data

| Derivatives | Concentration (mM) | Soaking time (days) | $d_{min}$ | No. of measurements | Unique data | Completeness (%) | $R_{merge}$* (%) |
|---|---|---|---|---|---|---|---|
| Native | | | 3.0 | 193,855 | 63,685 | 89.9 | 6.7 |
| Native (high resolution) | | | 2.8 | 301,392 | 76,703 | 88.9 | 10.8 |
| MMA (*c*-axis) | 1.0 | 3 | 3.5 | 102,143 | 38,506 | 85.8 | 6.9 |
| MMA (*a*-axis) | 1.0 | 5 | 3.5 | 115,572 | 39,325 | 87.4 | 7.9 |
| $HgCl_2$ | 0.5 | 3 | 3.5 | 113,997 | 39,943 | 88.9 | 7.0 |
| Thiomersal | 1.0 | 7 | 3.5 | 81,668 | 36,229 | 80.2 | 6.6 |
| $Pb(CH_3)_3Cl$ | 5.0 | 5 | 3.5 | 106,586 | 39,406 | 87.1 | 7.9 |
| $Pb(C_2H_5)_3Cl$ | 5.0 | 5 | 3.5 | 92,333 | 37,251 | 83.3 | 6.8 |
| $Tl(C_6H_5)_2Cl$ | 5.0 | 7 | 3.5 | 98,344 | 38,699 | 84.6 | 8.3 |

(*b*) Phase determination

| Derivatives | $R_{deriv}$ (%) | No. of sites† | $R_c$‡ | Phasing power at each resolution bin (Å) (10.5) | (8.2) | (6.7) | (5.7) | (4.9) | (4.3) | (3.9) | (3.5) | Total |
|---|---|---|---|---|---|---|---|---|---|---|---|---|
| MMA (*c*-axis) | 14.3 | 7 | 0.69 | 0.72 | 0.91 | 1.44 | 1.61 | 1.29 | 1.00 | 0.96 | 0.85 | 1.04 |
| MMA (*a*-axis) | 15.2 | 7 | 0.71 | 0.76 | 0.86 | 1.26 | 1.62 | 1.25 | 0.98 | 0.86 | 0.76 | 0.99 |
| $HgCl_2$ | 14.9 | 6 | 0.74 | 0.52 | 0.85 | 1.11 | 1.25 | 1.21 | 1.05 | 0.86 | 0.70 | 0.87 |
| Thiomersal | 16.3 | 9 | 0.71 | 0.76 | 0.91 | 1.49 | 1.57 | 1.15 | 0.88 | 0.92 | 0.76 | 1.00 |
| $Pb(CH_3)_3Cl$ | 14.2 | 5 | 0.76 | 0.78 | 1.00 | 1.16 | 1.28 | 0.95 | 0.73 | 0.56 | 0.52 | 0.81 |
| $Pb(C_2H_5)_3Cl$ | 16.2 | 5 | 0.73 | 0.53 | 0.71 | 0.81 | 1.04 | 0.99 | 0.76 | 0.63 | 0.61 | 0.73 |
| $Tl(C_6H_5)_2Cl$ | 16.8 | 5 | 0.80 | 0.52 | 0.94 | 1.13 | 1.07 | 0.83 | 0.54 | 0.46 | 0.36 | 0.64 |
| Figure of merit | | | | 0.84 | 0.91 | 0.89 | 0.82 | 0.71 | 0.56 | 0.44 | 0.34 | 0.58 |

**Crystallization.** Cocrystals of the conformation-specific antibody $F_v$ fragment 7E2 and the cytochrome *c* oxidase from *Paracoccus denitrificans* were obtained as described (C.O., S.I., B.L. and H.M., submitted). They belong to space group *P*4 with $a = b = 206.7$ Å, $c = 83.5$ Å, with one complex in the asymmetric unit. **Diffraction data.** X-ray data collection was carried out at station BL6A2 of the Photon Factory, Japan. Intensity data were obtained using a Weissenberg camera for macromolecular crystallography and imaging plates as detector[32]. Four crystals were used for native data collection and one for each heavy-atom derivative. For refinement, a high-resolution data set was collected up to 2.8 Å resolution using 8 crystals. Data for mercury derivatives were collected at 1.00 Å, and all other data at 0.94 Å. Data were processed with the HKL programs DENZO and SCALEPACK[33]. **Phasing.** Major heavy-atom sites were determined from difference Patterson maps and minor sites and relative positions of sites between derivatives were determined using the difference-Fourier technique. For these purposes a series of programs in the CCP4 suite was used[34]. MIRAS (multiple isomorphous replacement with anomalous scattering) phasing and refinement of the heavy-atom positions were done using the program MLPHARE[35]. MIRAS phases were calculated up to 3.5 Å resolution. The overall figure of merit was 0.58. **Density modification.** Because diffraction from the crystals showed a very large overall B-factor and high anisotropy, we had to apply an artificial overall B-factor to the intensity data to obtain an interpretable electron density map. The intensity data were scaled to the data of photosynthetic reaction centre at each resolution shell followed by an overall anisotropic B-factor application. Details of the method will be published elsewhere. The optimal modification was monitored with the free *R*-factor[36] obtained in the following density modification step. Density modification and phase extension to 3.0 Å was performed with the program DM[37]. Solvent flattening and histogram mapping were applied. The initial free *R*-factor was 0.461, but it reduced to 0.255 after 200 cycles. The best result was obtained with a solvent content of 75%. For further density modification, the program SOLOMON was used[38]. The *R*-factor dropped from 0.246 to 0.166 within 32 iterative steps of the modification. The best result again was obtained with a solvent content of 75%. **Model building and refinement.** The atomic model of the cytochrome *c* oxidase was built using the program O[39]. From the positions of the mercury binding sites and the sequences it became evident that it is the second gene[40] of subunit I from *Paracoccus denitrificans* which is expressed. As a model for the 7E2 $F_v$ fragment, the structure refined at 1.28 Å was used[41]. Simulated annealing followed by conventional positional refinement using the program X-PLOR[42] resulted in a structural model with an *R*-factor of 21.1% for the data between 6.0 and 2.8 Å resolution. The free *R*-factor of 5% of the data within the same resolution range was 25.6%. The root mean squares deviations from standard values of bond lengths and angles are 0.010 Å and 1.8°, respectively.

* $R_{merge} = \Sigma_h \Sigma_i |I_i(h) - \langle I(h) \rangle| / \Sigma_h \Sigma_i I_i(h)$, where $I_i(h)$ is the *i*th measurement.

† $R_{deriv} = \Sigma ||F_{PH}| - |F_P|| / \Sigma |F_P|$, where $F_{PH}$ and $F_P$ are protein and heavy-atom derivative structure factors, respectively.

‡ $R_c = \Sigma ||F_{PH} - F_P| - F_{H(calc)}|| / \Sigma |F_{PH} - F_P|$, $F_{PH}$ and $F_P$ are defined above, $F_{H(calc)}$ is the calculated heavy-atom structure factor. Summation is done using centric reflections only.

SU I–Tyr 280, which can form a hydrogen bond with SU I–His 276, and SU I–Trp 272, whose ring is in van der Waals distance parallel to SU I–His 326, may stabilize the $Cu_B$ site. The most interesting residue near $Cu_B$ is SU I–His 325. There is no electron density for its side chain, indicating disorder or multiple conformations. It can be modelled in at least two conformations (Fig. 4*d*). In one it forms bonds to $Cu_B$ and the $O_{\gamma 1}$ atom of SU I–Thr 344, whereas in the other it forms hydrogen bonds with the formyl group of haem $a_3$ and the carbonyl oxygen of SU I–Phe 340 and is not a $Cu_B$ ligand.

The planes of both haem groups are perpendicular to the membrane, and their interplanar angle is 108°. The shortest distance between the haem *a* and haem $a_3$ molecules is 4.7 Å, and the centre-to-centre distance is 13.2 Å. There are several possible pathways for electron transfer between the haems: (1) a direct pathway; (2) a pathway using the Fe-ligands SU I–His 413 (haem *a* Fe-ligand) and SU I–His 411 (haem $a_3$ Fe-ligand) by means of the connecting peptide backbone; and (3) one by means of SU I–Phe 412 and SU I–Met 416 with their side chains in contact to both haems.

## Proton pathways

For the function of cytochrome *c* oxidase, protons are required for two different purposes. 'Chemical' protons are consumed upon reduction of $O_2$ and water formation, and 'pumped' protons are translocated from the cytoplasmic to the periplasmic side of the membrane. Because the mutation SU I Asp 124 → Asn blocks proton pumping but not water formation, two separate pathways were expected[23,24]. In agreement with these results, two possible proton transfer pathways can be identified.

Pore B below haem $a_3$ (Fig. 5*a*) seems to be the pathway for consumed protons from the cytoplasmic surface to the oxygen binding site. The entrance is made up of a pit surrounded by SU I–loops IV–V and VI–VII, and the C-terminal extension (see Fig. 4*a*). The residues SU I–Ser 291, SU I–Lys 354, SU I–

Thr 351, the hydroxyl group of haem $a_3$ and SU I–Tyr 280 sequentially contribute to this pathway. With one exception, these residues are connected by hydrogen bonds directly, or possibly, as indicated by unexplained electron density, by a solvent molecule. SU I–Tyr 280 might donate the proton to the oxygen. The exception is SU I–Lys 354, which does not form hydrogen bonds, either to SU I–Ser 291 or to SU I–Thr 351. Because the environment of this lysine residue is completely hydrophobic, it should be deprotonated. In other possible conformations it could form hydrogen bonds to SU I–Ser 291 or SU I–Thr 351.

The lower half of pore A and presumably the upper part of pore B form the pathway for the pumped protons (Fig. 5*a*). A gap between SU I–loops II–III and III–IV allows access to the entrance of the pathway. Near the entrance, residues SU I–Asp 124, SU I–Thr 203 and SU I–Asn 199 form a gate. The residues SU I–Asn 113 and SU I–Asn 131 follow. Replacement of one of them by hydrophobic ones blocks proton pumping[24]. Beyond SU I–Tyr 35 a cavity, primarily lined up with hydrophilic residues such as SU I–Ser 193, is found. Electron density for several solvent molecules in hydrogen-bond distances are visible leading to SU I–Glu 278. Interruption of the regular helical structure of transmembrane segment SU I–TM II by SU I–Pro 105 allows the access of protons to SU I–Glu 278.

Beyond SU I–Glu 278 the proton pathway is less clear. There are two possibilities. First, it might lead into pore B and reach the $Cu_B$-ligand SU I–His 325. The regular hydrogen-bonding pattern of transmembrane segment SU I–TM VI is interrupted in this area, partly as a result of SU I–Pro 277. The carbonyl oxygen atoms not involved in a helical hydrogen-bonding pattern might play an important role in proton conductance by binding solvent molecules. As mentioned above, SU I–His 325 might possess at least two alternative conformations. A switch between these two conformations might allow conduction of protons to the formyl group of haem $a_3$, the carbonyl oxygen of SU I–Leu 393, and SU 1–Asp 399. The residue SU 1–Asp 399, might be important in accepting protons from SU I–His 325. Alternatively, a direct proton transfer from SU I–Glu 278 to one of the haem $a_3$ propionates might be possible. Upon conformational changes these side chains could approach one another to hydrogen-bonding distance.

A cleft between SU I and SU II could be the exit pathway for the pumped protons. This cleft is hydrophilic owing to the presence of polar side chains in the SU I–loop VII–VIII, the horizontal helix in the loop IX–X, transmembrane helix II of SU II and SU II-strand 7. Nearby a negative charge cluster consisting of SU I–Asp 399, one proprionate group of haem $a_3$, SU I–Asp 404, SU II–Asp 193, and SU II–Glu 218 exists. Su I–His 403 is placed in the centre of this cluster. The residues homologous to Su I–His 403 and SU I–Asp 404 have been postulated to be part of a Mn/Mg binding site[25]. We could not find sufficient electron density for Mn, but weaker densities next to SU I–His 403 might be caused by a Mg atom and/or solvent molecules.

## Mechanism of proton pumping

As outlined above, the most likely pathway for the pumped protons includes SU I–His 325 with two possible conformations related to proton conduction. This observation suggests that $Cu_B$ and its ligand SU I–His 325 might play a crucial role in proton pumping. In an attempt to couple the chemistry of oxygen reduction directly to proton pumping of the terminal haem–copper-oxidases, a 'histidine cycle' mechanism has previously been suggested[26,27]. Here we propose a mechanism in which SU I–His 325 cycles through the imidazolate, imidazole and imidazolium states, and shuttles between two positions (Fig. 5*b*). This mechanism also obeys the principle of electroneutrality of redox and ligand state changes around the binuclear centre with charge compensations provided only by protonation reactions[28,29]. Figure 5*c* shows a short version of our 'histidine cycle/shuttle' mechanism. In state 1, the oxidized or O-state, SU I–His 325 is in the imidazolate state, owing to positive charges on the Fe and Cu atoms, and bound to $Cu_B$. Its negative charge is further stabilized by accepting a hydrogen bond from SU I–Thr 344. During single reduction of the binuclear centre a proton is taken up by the pump pathway to maintain electroneutrality, and converts the side chain of SU I–His 325 to the neutral imidazole form. The imidazole ring is now a hydrogen bond donor to Su I–Thr 344 (state 2). During the second reduction another proton is taken up, again by the pump pathway, and will be bound to SU I–His 325. However, this is not possible as long as this residue is a $Cu_B$-ligand. Therefore it rotates to its alternative binding site, accepting the proton during rotation. Molecular oxygen is bound to the haem $a_3$-Fe atom and the so-called compound A is formed (state 3). Upon further reduction the peroxy (P)-state 4 is created (see ref. 1 for review). For charge compensation, a proton has to be taken up. However, because there is no other group with an appropriate pK in the immediate environment available (and accessible from the pump pathway), SU I–Glu 278 is most likely to take up the proton. The chemistry of oxygen reduction then requires the double protonation of the peroxy form, formation of water and creation of the oxoferryl state 5 (F). To keep the overall charge around the binuclear centre constant, the two protons bound to Su I–His 325 have to be released. They are ejected into the exit pathway towards the periplasm. The side chain of SU I–His 325 rotates back. In the imidazolate form it is able to accept the proton from Su I–Glu 278, and it can be bound to $Cu_B$ and SU I–Thr 344 as in state 2. Formation of state 6 occurs analogous to formation of state 3. Two further protons are then taken up by the pathway for protons to be consumed, and water is formed again. The two protons of the SU I–His 325 imidazolium will be ejected by the exit pathway. The side chain of SU I–His 325 swings back and the cycle is now closed.

In the cycle pumped protons are taken up first, and they are ejected by the protons needed for water formation. These two types of protons are provided separately by the two different pathways (Fig. 5*b*). The delay of the arrival of the protons to be consumed might be explained by the presence of SU I–Lys 354 in their pathway because a conformational change and an energetically unfavourable protonation of this lysine side chain would be necessary for proton transfer.

One objection against this mechanism is that in *bo*-type and *cbb*-type terminal oxidases, the haem does not possess a formyl group to form the hydrogen bond to SU I–His 325. This is not a serious problem, as SU I–His 325 could directly form a hydrogen bond to the carbonyl oxygen of SU I–Leu 393 or to SU I–Asp 399. However, we cannot exclude the possibility that the lack of electron density for the side chain of SU I–His 325 has nothing to do with proton pumping, but is an artefact of the crystallization conditions, especially of the presence of ammonium and azide. It also could be related to the 'resting', 'pulsed', 'slow' and 'fast' states of the enzyme (see, for example, ref. 31). Alternatively, protons might reach the negative charge cluster by the pump channel during the reduction of the binuclear centre and stay there until they are ejected by the exit pathway by long-range electrostatic repulsion by the protons consumed in water formation.

It is evident that further experiments, especially spectroscopic, theoretical and crystallographic studies on wild-type cytochrome *c* oxidase and site-directed mutants, are needed to test the various mechanisms. The cytochrome *c* oxidase from *Paracoccus denitrificans* offers unique possibilities for this purpose. □

Received 19 July; accepted 3 August 1995.

1. Babcock, G. T. & Wikström, M. *Nature* **356,** 301–309 (1992).
2. Saraste, M. *Q. Rev. Biophys.* **23,** 331–366 (1990).
3. Calhoun, M. W., Thomas, J. W. & Gennis, R. B. *Trends biochem. Sci.* **19,** 325–330 (1994).
4. Kadenbach, B., Kuhn-Nentwig, L. & Büge, K. *Curr. Topics Bioenerg.* **15,** 113–161 (1987).
5. Haltia, T. *Biochemistry* **33,** 9731–9740 (1990).
6. Caughey, W. S. *et al. J. Bioenerg. Biomembr.* **25,** 81–92 (1993).

7. Ludwig, B. & Schatz, G. *Proc. natn. Acad. Sci. U.S.A.* **77,** 196–200 (1980).
8. Hendler, R. W., Pardhasaradhi, K., Reynafarje, B. & Ludwig, B. *Biophys. J.* **60,** 415–423 (1991).
9. Haltia, T. *et al. EMBO J.* **8,** 3571–3579 (1989).
10. Pascher, I., Lundmark, M., Nyholm, P.-G. & Sundell, S. *Biochim. biophys. Acta* **1113,** 339–373 (1992).
11. Haltia, T., Saraste, M. & Wikström, M. *EMBO J.* **8,** 2015–2021 (1991).
12. Turba, A., Jetzek, M. & Ludwig, B. *Eur. J. Biochem.* **231,** 259–265 (1995).
13. Adman, E. T. *Adv. Protein Chem.* **42,** 145–197 (1991).
14. Steffens, G. J. & Buse, G. *Hoppe-Seyler's Z. physiol. Chem.* **360,** 613–619 (1979).
15. Guss, M., Bartunik, H. D. & Freeman, H. C. J. *Acta crystallogr. B* **48,** 790–811 (1992).
16. Steffens, G. C. M., Soulimane, T., Wolff, G. & Buse, G. *Eur. J. Biochem.* **213,** 1149–1157 (1993).
17. Kelly, M. *et al. J. biol. Chem.* **268,** 16781–16787 (1993).
18. Antholine, W. E. *et al. Eur. J. Biochem.* **209,** 875–881 (1992).
19. Blackburn, N. J. *et al. Biochemistry* **33,** 10401–10407 (1994).
20. van der Oost, J. *et al. EMBO J.* **11,** 3209–3217 (1992).
21. Rieder, R. & Bosshard, H. R. *J. biol. Chem.* **255,** 4732–4739 (1980).
22. Hosler, J. P. *et al. J. Bioenerg. Biomembr.* **25,** 136–143 (1993).
23. Thomas, J. W. *et al. Biochemistry* **32,** 10923–10928 (1993).
24. Garcia-Horsman, J. A., Puustinen, A., Gennis, R. B. & Wikström, M. *Biochemistry* **34,** 4428–4433 (1995).
25. Hosler, J. P., Espe, M. P., Zhen, Y., Babcock, G. T. & Ferguson-Miller, S. *Biochemistry* **34,** 7586–7592 (1995).
26. Wikström, M. *et al. Biochim. biophys. Acta* **1187,** 106–111 (1996).
27. Morgan, J. E., Verkhovsky, M. I. & Wikström, M. *J. Bioenerg. Biomembr.* **26,** 599–608 (1994).
28. Mitchell, R. & Rich, P. R. *Biochim. biophys. Acta* **1186,** 19–26 (1994).
29. Rich, P. R. *Aust. J. Pl. Physiol.* **22,** 479–486 (1994).
30. Wikström, M. *Nature* **338,** 776–778 (1989).
31. Moody, A. J., Cooper, C. E. & Rich, P. R. *Biochim. biophys. Acta* **1059,** 189–207 (1991).
32. Sakabe, N. *J. appl. Crystallogr.* **16,** 542–547 (1983).
33. Otwinowski, Z. in *Proc. CCP4 Study Weekend, 29–30 Jan 1993, Data collection and Processing* (eds Sawer, L., Isaacs, N. & Bailey, S.) 56–62 (SERC Daresbury Laboratory, Warrington, 1993).
34. Collaborative Computational Project, Number 4. *Acta crystallogr. D* **50,** 760–763 (1994).
35. Otwinowski, Z. in *Proc. CCP4 Study Weekend, 25–26 Jan 1991, Isomorphous Replacement and Anomalous Scattering* (eds Wolf, W., Evans, P. R. & Leslie, A. G. W.) 80–86 (SERC Daresbury Laboratory, Warrington, 1991).
36. Brünger, A. T. *Nature* **355,** 472–475 (1992).
37. Cowtan, K. in *Joint CCP4 and ESF-EACBM Newsletter on Protein Crystallography* **31,** 34–38 (1994).
38. Abrahams, J. P., Leslie, A. G. W., Lutter, R. & Walker, J. E. *Nature* **370,** 621–628 (1994).
39. Jones, T. A., Zou, J. Y., Cowan, S. W. & Kjeldgaard, M. *Acta. crystallogr. A* **47,** 110–119 (1991).
40. Raitio, M., Pispa, J. M., Metso, T. & Saraste, M. *FEBS Lett.* **261,** 431–435 (1990).
41. Essen, L. O. thesis. Johann Wolfgang Goethe-Univ. (1995).
42. Brünger, A. T., Kuriyan, J. & Karplus, M. *Science* **235,** 458–460 (1987).
43. Kabsch, W. & Sander, C. *Biopolymers* **22,** 2577–2637 (1983).
44. Kraulis, P. J. *J. appl. Crystallogr.* **24,** 946–950 (1991).
45. Bacon, D. J. & Anderson, W. F. *J. molec. Graphics* **6,** 219–220 (1988).
46. Merrit, E. A. & Murphy, M. E. P. *Acta crystallogr. D* **50,** 896–873 (1994).


ACKNOWLEDGEMENTS. We thank the staff of the synchrotron facilities at the Photon Factory, Tsukuba, Japan, and at the ESRF, Grenoble, France for help; J. Eich, C. Münke and in particular H. Müller for technical assistance; and C. R. D. Lancaster for reading the manuscript and discussions. S.I. was supported during part of this work by a grant from the Human Science Frontier Programme, and C.O. by a grant from the Fonds der Chemischen Industrie. Financial support was obtained from the Max-Planck-Gesellschaft, the Deutsche Forschungsgemeinschaft (SFB 167) and the Fonds der Chemischen Industrie. H.M. and S.I. are members of the TARA project of Tsukuba University, Japan. The coordinates will be deposited in the Brookhaven Protein Data Bank (PDB).

LETTERS TO NATURE

# Slow rotation of the Sun's interior

**Y. Elsworth*, R. Howe*, G. R. Isaak*, C. P. McLeod*, B. A. Miller*, R. New†, S. J. Wheeler* & D. O. Gough‡**

* School of Physics and Space Research, University of Birmingham, Edgbaston B15 2TT, UK
† School of Science, Sheffield Hallam University, Sheffield S1 1WB, UK
‡ Institute of Astronomy and Department of Applied Mathematics and Theoretical Physics, Madingley Road, Cambridge CB3 0HA, UK, and JILA, Campus Box 440, Boulder, Colorado 80309-0440, USA

**THE rotation of the Sun is not that of a rigid body; at its surface, the gas near the poles has a lower angular velocity than that near the equator[1]. This latitudinal variation persists to the base of the convection zone, below which the angular velocity becomes approximately uniform[2,3]. Any variations of angular velocity at much greater depths are, however, poorly constrained[4–10]. Observations of solar oscillation modes have been used to probe density variations in the Sun; rotational splitting of degenerate modes, although difficult to resolve, provides important constraints on the dynamical structure[11]. Here we report observations of rotationally split modes made over a three-year period with the Birmingham Solar Oscillations Network. Our results indicate that there is a substantial region inside the Sun that is rotating more slowly than the surface. This situation seems likely to be transient—the minimum-energy state would have all the deeper regions rotating with the same angular velocity—and is at variance with our current ideas about the rotational evolution of main-sequence stars[12]. We have no solution to the dynamical problem this poses.**

The oscillations that we observe are resonant acoustic waves, called p modes. The eigenfunction of a mode varies in the horizontal approximately as a spherical harmonic $Y_l^m$ of degree $l$ and azimuthal order $m$, and is characterized also by a principal quantum number $n$, called the order, which is associated with the radial variation. Eigenfrequencies $\nu_{nl,m}$ would be degenerate with respect to $m$ if the Sun were spherically symmetrical, but rotation shifts the frequencies by a small amount $\delta\nu_{nl,m}$ which is very nearly an odd function of $m$, provided that the axis of $Y_l^m$ coincides with the axis of rotation. A magnetic field, or any other symmetry-breaking agent that cannot distinguish east from west, shifts $\nu_{nl,m}$ by an even function of $m$. Acoustic waves propagate downwards from the reflecting surface layers of the Sun and are refracted back by the rising sound speed. Evidently $\nu_{nl,m}$ depends on conditions only in the region of the Sun within which the waves propagate. The depth of penetration increases as $l$ decreases. The Birmingham Solar Oscillations Network observes the modes of lowest degree, and therefore senses as deeply as it is possible to do with p modes.

Inversions[2,3,13] of splitting data from modes of intermediate degree have provided a fairly robust view of the Sun's angular velocity $\Omega(r, \theta)$ at radii $r > 0.5\,R_\odot$. Broadly speaking, the photospheric variation of $\Omega$ with colatitude $\theta$ persists through the convection zone, at the base ($r = r_c \approx 0.713 R_\odot$) of which is an abrupt unresolved transition to nearly uniform $\Omega$. The value, $\Omega_c$, of $\Omega$ immediately beneath the transition ($\Omega_c/2\pi \approx 440$ nHz) is such that the mean specific angular momentum, averaged over spherical shells, is constant through the transition[3,14,15] suggesting that there is no net torque exerted across the transition, which is consistent with a steady state. But opinions based on low-degree data about what happens beneath $r = 0.5\,R_\odot$ are diverse, some[4–7] being that rotation is relatively rapid, others[8–10,13] that $\Omega \approx \Omega_c$. Here we accept the inversions in and immediately beneath the convection zone, and we use our new observations to calibrate a simple model of $\Omega$ at greater depths.

A severe difficulty previously encountered in measuring splitting of low-degree modes arises from the fact that the widths of the lines in the power spectrum are comparable with the splitting; the lines of the components with different $m$ of a $(n, l)$ multiplet are therefore blended, and it is necessary to rely on statistical cancellation of interference effects to infer the splitting indirectly, with risk of biased estimation. We have overcome that difficulty by observing low-frequency modes whose lines are narrow enough for the individual components of a multiplet to be resolved, permitting a direct measurement of the splitting. This has never before been achieved with whole-disk observations.

Observations were made with a network of six resonance-scattering spectrometers located in Tenerife, Chile, California, Eastern Australia, Western Australia and South Africa. With such a global network the confusing effects of daily sidelobes in